Emission Characteristics of Passively Fed Electrospray Microthrusters with Propellant Reservoirs

Citation: Krejci, David et al. "Emission Characteristics of Passively Fed Electrospray Microthrusters with Propellant Reservoirs." Journal of Spacecraft and Rockets 54.2 (2017): 447–458.

As Published: http://dx.doi.org/10.2514/1.A33531

Publisher: American Institute of Aeronautics and Astronautics

Persistent URL: http://hdl.handle.net/1721.1/108538

Version: Author's final manuscript: final author's manuscript post peer review, without publisher's formatting or copy editing

JOURNAL OF SPACECRAFT AND ROCKETS
Vol. 54, No. 2, March–April 2017

Emission Characteristics of Passively Fed Electrospray Microthrusters with Propellant Reservoirs

David Krejci* and Fernando Mier-Hicks†
Massachusetts Institute of Technology, Cambridge, Massachusetts 02139
Robert Thomas‡ and Thomas Haag§
NASA John H. Glenn Research Center, Cleveland, Ohio 44135
and
Paulo Lozano¶
Massachusetts Institute of Technology, Cambridge, Massachusetts 02139

DOI: 10.2514/1.A33531

The characterization of a miniaturized ionic liquid electrospray thruster for nanosatellite applications is presented. The thruster investigated features an emitter array of 480 emitter tips per square centimeter and a 1 cm^3 propellant tank with an entirely passive propellant supply; it is operated at a power level of less than 0.15 W. The paper presents energy- and mass-resolving beam spectroscopy of the packaged thruster system, as well as two independent thrust measurements. This allows derivation of thruster performance parameters under realistic firing conditions, including individual thruster efficiency contributions, specific impulse, and thrust. The total thruster efficiencies of 36%; specific impulse of ~760 s, including all losses; and thrust of 11–12.5 μN are presented at emission currents of 150 μA for a device of ~1 cm^2. The current emission data without current decay of ~90 h are presented with a maximum of 172 h.

Nomenclature

F	=	force, N
$f(\Phi)$	=	current distribution function
f_i	=	ion current fraction
g_0	=	standard acceleration due to gravity, m/s^2
I	=	current, A
I_{em}	=	emitted current, A
I_{sp}	=	specific impulse, s
I_{sp}^{ideal}	=	loss-free specific impulse, s
L	=	drift length, m
m	=	mass, kg
$\dot{m}$	=	mass flow, kg/s
q/m	=	charge-to-mass ratio, C/g
T	=	thrust, N
t	=	time, s
V_B	=	effective beam acceleration potential, V
V_e	=	emitter potential, V
V_{ex}	=	extractor potential, V
η	=	efficiency
Φ	=	beam opening half-angle, deg

Subscripts

E	=	energy
i	=	ionization
P	=	polydispersive
RPA	=	retarding potential analyzer
ToF	=	time of flight
tr	=	transmission
Φ	=	angular

Received 3 December 2015; revision received 9 November 2016; accepted for publication 15 November 2016; published online 31 January 2017.

*Research Scientist, Department of Aeronautics and Astronautics, 77 Massachusetts Avenue; krejci@mit.edu. Member AIAA.
†Ph.D. Candidate, Department of Aeronautics and Astronautics, 77 Massachusetts Avenue.
‡Research Engineer, In-Space Propulsion Systems, 21000 Brookpark Rd. Member AIAA.
§Aerospace Engineer, In-Space Propulsion Systems, 21000 Brookpark Rd. Member AIAA.
¶Professor, Department of Aeronautics and Astronautics, 77 Massachusetts Avenue. Member AIAA.

I. Introduction

HIGH-EFFICIENCY propulsion is considered as an enabling technology in the growing field of nanosatellites with advanced scientific and commercial missions, allowing formation flight, orbit change maneuvers, and active deorbiting, among others [1]. The thruster presented in this work is a miniaturized, efficient electrostatic electrospray thruster based on microelectromechanical systems (MEMS) fabrication processes, complying with stringent volume, mass, and power requirements imposed by nanosatellites.

Electrospray thrusters are a class of electric thrusters that produce thrust by acceleration of ions or droplets after extraction from an electrically conductive liquid surface under an applied electrostatic field. To minimize thruster potentials necessary to achieve the local field strength necessary for charged particle extraction from the liquid bulk, the propellant is typically applied onto a field enhancing structure, such as a needle or sharp emitter tip, in conjunction with a high-voltage extraction grid, as shown in Fig. 1. In the process of ion, or droplet, extraction by electric fields, the liquid deforms into a sharp cone-shaped meniscus, equilibrating electrical pull and surface tension and upstream pressure. The increased electric field strength at the cone tip leads to the extraction of charged particles, which are then accelerated to produce thrust [2]. Typically, two regimes of operation, or a mixture of these, occur: the cone-jet regime, in which the meniscus breaks up into droplets [3]; and the ionic regime with pure ion extraction and accordingly higher specific impulse [4,5]. The ionic mode is obtained by using ionic liquids as propellant, which are room-temperature molten salts consisting of chemically stable mixtures of positive and negative charges. Spacecraft charging is avoided by firing in module pairs with opposite charge and alternating the polarity periodically to maintain chemical balance and prevent electrochemical decay [6]. Due to the negligible vapor pressure of the ionic liquids [7], there is no need for propellant pressurization. These electrospray thrusters therefore allow for passive feed systems, rendering hard-to-miniaturize components such as valves unnecessary, and lend themselves well toward miniaturization [4]. Electric thrusters generally feature high specific impulse values compared to chemical thrusters because propellant

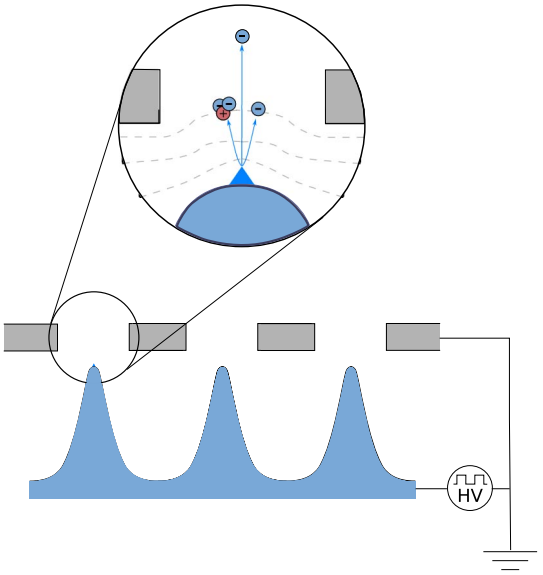

Fig. 1 Electrospray principle with charged particle extraction from menisci on top of porous emitter structures.

exit velocities are not limited to chemically storable energy. However, miniaturized electric thrusters usually feature low thrust levels. To increase thrust, arrays of emitters have been proposed and successfully tested [8–15]. The possibility of ion emission, as opposed to droplet emission, for the ionic liquid EMI–BF_4 (1-Ethyl-3-methylimidazolium tetrafluoroborate) was experimentally shown using spectrometric characterization measurements [16–18].

In this work, we present the characterization of the emission from porous emitter arrays featuring 480 emitter tips for fully packaged, highly miniaturized thrusters. Studies on performance characterization focusing on measurements taken directly after wetting of the emitter substrates are available [12,19], including characterization of devices on different thrust stands [15]. This study is dedicated to characterizing emission under realistic firing conditions of a thruster, including a fully sized propellant reservoir to ensure steady-state propellant distribution and sustaining emission over extended time periods. We present spatially and energy-resolving beam measurements and time-of-flight analyses of the emitted particle beam. In addition, we present independent direct thrust measurements. This allows us to draw conclusions on the state of the emission, characterize thruster performance parameters such as thrust efficiency and specific impulse, and provide a baseline of a complete propulsion system that could help guide future developments.

II. Description of the Microthruster

The microthrusters investigated in this study consist of an array of 480 emitter tips, manufactured by laser ablation out of a single piece of porous glass with an approximate footprint of 1×1 cm, arranged in a triangular pattern [20,21] with an average emitter tip height of 175 μm. The emitter tips have an apex radii of approximately 15 μm, and pore sizes are typically found between 1 and 10 μm. An optical image of the emitter tip structures is shown in Fig. 2a. This emitter chip is bonded to a silicon frame used for packaging and alignment of the emitter structures. This square silicon packaging frame features four corner posts with an insulating Pyrex layer to electrically insulate the high potential emitter grid from the extractor grid. The latter is attached to the corner posts of the frame, allowing for alignment of the individual apertures to the emitter tips. Optical investigation of the emitter tips in the array confirm emitter tip heights of 160–175 μm. The apexes of the tips are aligned in the same plane as the lower plane of the extractor grid, for which the apertures are 300 μm in diameter. Typical alignment accuracy is found to be better than 25 μm. This emitter–extractor package is then bonded to a propellant tank manufactured in Polyether ether ketone, as shown in Fig. 2b. The tank houses a distal electrode, manufactured from

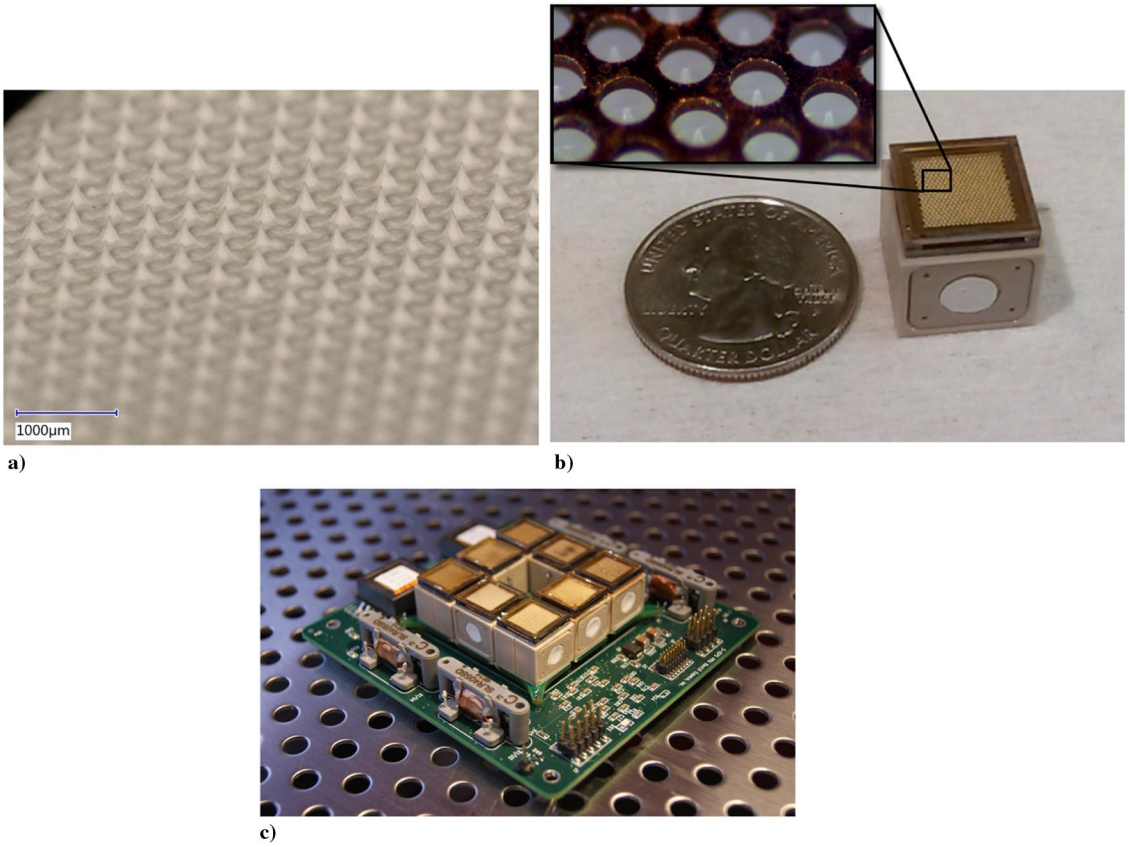

Fig. 2 Images of iEPS thrusters: a) optical image of porous emitter array with 480 emitter tips, b) fully packaged thruster with 1 ml tank volume, and c) fully integrated S-iEPS unit including power supply.

pyrolyzed carbon aerogel [22,23] with a large internal surface area. Propellant supply flow is managed passively by capillary forces only. Loading the thruster with ionic liquid is performed in vacuum after outgassing of both the liquid and the thruster to avoid gas trapping, which could trigger discharges during thruster operation [24]. EMI–BF_4 is used as the standard propellant throughout this study, unless otherwise indicated. The thrusters investigated in this work are the building blocks of the scalable ion electrospray propulsion system (S-iEPS), which is a CubeSat-sized propulsion unit developed under the NASA Microfluidic Electrospray Program (MEP) [25], fitting in an envelope of less than 200 cm^3. An image of the fully integrated unit is shown in Fig. 2c.

III. Methods

A. Emission Current and Interception

Emission behavior in terms of emitted current as a function of applied emitter potential was determined by applying three successive voltage scans in a triangular profile over the investigated voltage range, with a period of 60 s. High voltage was generated and measured using a Matsusada AP-3B1-L2 with ± 1 V accuracy in the voltage monitor. Both the emitted current, which is the current drawn by the emitter from the laboratory power supply, and the intercepted current, which is defined as the current measured from the extractor to ground, were recorded by measuring the voltage drop across a 1 kΩ resistor in conjunction with an isolation amplifier (Analog Devices AD210JN) leading, after calibration with resistive load, to a measurement accuracy of ± 0.1 μA. Averaging of the recorded data was performed, incorporating error propagation.

B. Energy Distribution

A retarding potential analyzer (RPA) was used to measure the energy distribution of the charged particle beam using a singly charged species approximation for the beam. The RPA instrument consisted of a Faraday cup of a 1/4 in. (6.35 mm) aperture, with a grounded entrance grid, followed by the retarding potential grid and a bias grid for electron repulsion upstream of the Faraday cup. The instrument schematic is shown in Fig. 3a. The RPA detector was, if not mentioned otherwise, positioned directly at the emitter's central thrust axis at a distance of 60 mm from the extractor grid. Measurements were performed by operating the emitter in single polarity, with 20 successive scans of the retarding potential from zero to the emitter potential incremented by 100 V, both increasing and decreasing, with a period of 20 s. Recorded data were then reduced by averaging over all scans, incorporating error propagation. The current was measured using a Keithley 6514 electrometer with femtoampere accuracy. The largest error contribution in this experiment was found in the voltage ripple of the retarding grid of nominally $\pm$ 5 V.

C. Spatial Beam Distribution

The spatial beam distribution was recorded using the same Faraday cup as described in Sec. III.B, which was mounted on a rotary arm 60 mm from the extractor surface and able to move from –90 to +90 deg from the central thrust axis. The rotary motion was controlled by an electric motor in conjunction with a solid shaft rotary feedthrough and position switches at $\pm$90 deg. The measurement principle is shown in Fig. 3a, with the RPA grid grounded. The angular position was read using an incremental angular encoder with 2500 counts per revolution. Typically, 20 scans over the entire hemisphere were performed with the thruster being continuously operated in single polarity at the stated current, with data being reduced by averaging, thereby incorporating error propagation. The current was measured using a Keithly 6514. The main source of error in this measurement was an offset present when aligning the thruster with the rotation instrument's zero axis upon thruster mounting, which was measured as less than 5 deg. The error introduced by approximating the finite dimensions of the emitter as a point source was estimated to be less than 2.5 deg.

D. Mass Distribution

Knowledge on the mass distribution of the emitted ion beam allowed the identification of relative fractions of charged ions, solvated ions, droplets, or products from fragmentation events in the beam, allowing the determination of the average charge-to-mass ratio of the emitted beam, and thus the specific impulse. To determine the beam composition, the time-of-flight (TOF) measurements were performed in a large vacuum chamber facility (1.5 × 1.6 m, cryopumped, with a pumping speed of 7000 l/s of xenon and a chamber base pressure less than 5×10^{-6} torr) to minimize chamber effects. Figure 3b shows a schematic of the TOF setup used, with a free drift length of 1.6 m between the collector and the electrostatic gate. The collector consisted of a grounded grid, succeeded by a bias grid to suppress secondaries, and a detector plate with a 20 cm diameter, made out of copper. The sides of the entire collector structure were shielded from ambient charges. A stopping gate configuration was used to interrupt the emitted ion beam. In this configuration, the gate was switched to a potential higher than the emitter potential using a fast square waveform, therefore interrupting the beam of charged particles. The electrostatic gate consisted of a series of three highly transparent grids, with the high-voltage pulse (960 V) applied to the center grid, enclosed by grounded grids up- and downstream to ensure a potential free drift zone. The signal was

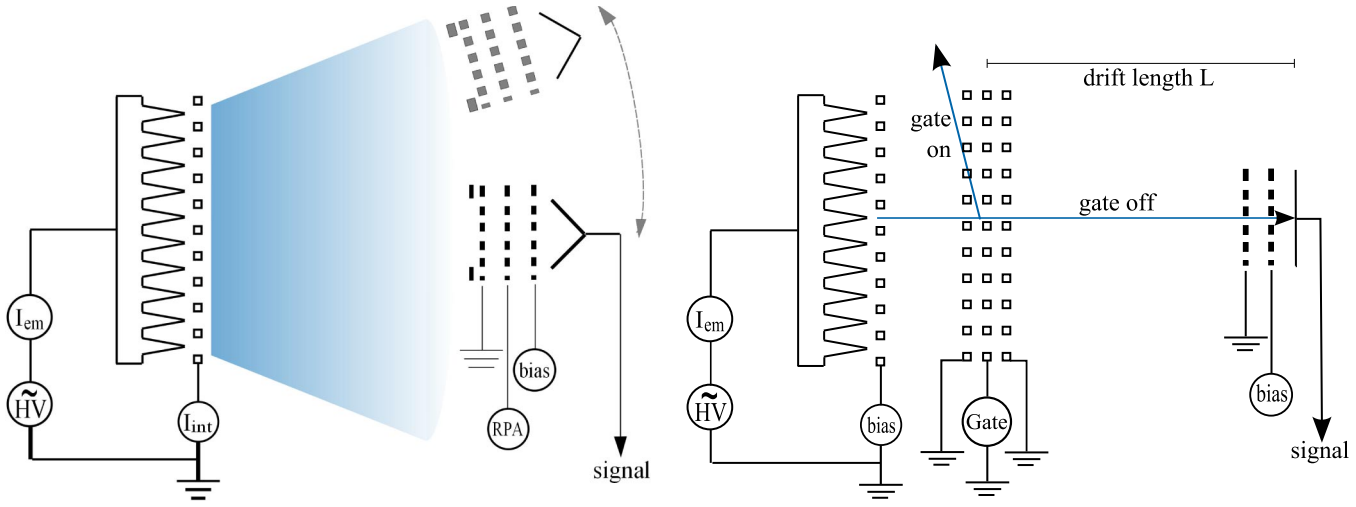

a) RPA and spatial beam distribution measurement

b) Time-of-flight measurement

Fig. 3 Experiment configurations.

amplified by a custom-made transimpedance amplifier and recorded by an oscilloscope (Agilent Technologies DSO-X 3024A) set to 2000 trace averaging. The main uncertainty in this measurement for determining the specific impulse originated from the signal noise obstructing the trailing edge of the low-velocity particles. A detailed discussion on an approach used to overcome this issue and the resulting measurement accuracy is given in Sec. V.A.1.

E. Extended Testing

During extended duration experiments, the applied emitter polarity was alternated using a period of 30 s to avoid charge imbalance in the propellant reservoir. The average specific impulse was determined by conducting tests with relatively long firing durations, with continuous recording of time traces of applied potential, as well as emitted and intercepted currents, allowing integration of the net emitted current with an accuracy of ± 0.1 μA. Propellant consumption was determined as the difference in weight of the packaged thruster before and after the test. Humidity intake before the test was avoided by storage in a controlled low-humidity (less than 20%) environment before weight determination, as well as by determining the weight right after venting of the vacuum chamber. Applicable measurement accuracies include the current monitor accuracy (± 0.1 μA) and the measurement uncertainty of the scale of 0.1 mg.

F. Thrust

Two different configurations were used for independent direct thrust measurements:

1. *Massachusetts Institute of Technology CubeSat Testbed*

This thrust measurement was based on a magnetically levitated satellite mockup containing a power supply and two thrusters in a rotational thrust configuration. The rotational position and movement of the levitated satellite were monitored and used, in conjunction with the knowledge of the inertia of the system, to determine the thrust exerted by the two thrusters. This setup included an eddy current break to counteract and desaturate rotational movement, as well as a charge sensor to investigate eventual power processing unit ground drift. A detailed description of this measurement configuration as well as achievable accuracies can be found in [26]. The total measurement uncertainty of this instrument was calculated from individual measurement inaccuracies, including sufficient margin, as ± 1 μN. Uncertainty in high side emission current measurements were conservatively estimated at 10%, including measurement uncertainty and current drifts due to long measurement durations. Measurements were performed in a 1.5×1.6 m, cryopumped vacuum chamber (pumping speed of 7000 l/s of xenon) with a base pressure of less than 5×10^{-6} torr and included thrusting times of 20 min for each emission current setting.

2. *NASA Thrust Balance*

This setup consisted of a torsional-arm balance, with thrust being a function of a known spring constant and the arm displacement. A counterweight was placed at the opposite end of the arm from the testbed, which minimized gravitational influence on the thrust balance. The arm displacement was measured by a linear variable differential transformer with a resolution of ± 2 μm [27]. The measured force was calibrated in situ and under vacuum before each test sequence. Three free-hanging weights, each with a mass of 3.1 mg, were strung on a fiber and passed over a pulley to align the calibration force with the axis of the testbed. Oscillation of the thrust balance arm was damped with a small solenoid magnet driven by a differential amplifier. Gain of the amplifier was normally tuned to achieve critical damping, but it could be switched off as needed to allow undamped isolation of the balance. To minimize uncertainty due to drift in the thrust signal, the thruster was turned off between throttle points to recheck the datum point. The thrust balance was operated in a cylindrical chamber of 1.5 m in diameter and 4.5 m in length, which was evacuated by four oil diffusion pumps with a background pressure of 9.7×10^{-7} torr. Multiple measurements have been performed for each current setting, with a resulting measurement uncertainty of less than 6% for the tests presented in Sec. IV.C.6.

IV. Results

A. Description of Measurements, Measurement Protocols, and Test Matrix

Investigations of the full emitter (Sec. IV.C) were performed for the packaged thruster including the propellant tank to ensure constant emission properties throughout extended experiment durations. In this configuration, the propellant tank was filled with ionic liquid, and the high voltage was contacted to the liquid using porous distal electrodes. Only the TOFs of the full-array and single-emitter experiments (Sec. IV.B) were conducted without a dedicated propellant supply because total propellant consumption was small. In these tests, a small amount of propellant was stored in a piece of microfiber glass attached to the backside of the glass chip, mimicking the propellant supply of a fully packaged thruster.

Each emitter was subjected to a conditioning procedure at initial startup to ensure uniform propellant distribution. This propellant priming procedure consisted of applying a voltage about 50% larger than the expected nominal value during a period of about 10–20 min. These values depended on the specific geometry and surface wetting condition of the thruster array. After stable emission was achieved, which was defined as the absence of apparent change in emission current for constant applied emitter potential over multiple polarity switching cycles, the thruster's emission characteristic was determined by recording the emission currents as a function of applied emitter potential, as discussed in Sec. III.A. Characterization experiments were performed at an emission current of $I_{em} = 150$ μA, which was a value determined primarily by the NASA MEP requirement of 100 μN for the full propulsion system[**] and the low fraction of intercepted to emitted current found for this operational point. This corresponded to an average emission current of ~300 nA per emitter tip, which was consistent with the single-emitter operation per tip. Although emitters were typically operated in a single polarity during most characterization experiments described in Sec. III (including spatial beam distribution, RPA and TOF measurements), a polarity alternation scheme with switching periods of 30 s was typically employed during long-duration operations to avoid electrochemical decay.

The propellants EMI–BF_4 and EMI-DCA (1-Ethyl-3-Methylimidazolium Dicyanamide) were purchased from Ionic Liquids Technologies, Inc., with purities of ≥97.0% and ≥98.5%, respectively. EMI–$GaCl_4$ (1-Ethyl-3-Methylimidazolium Tetrachlorogallate) was synthesized in house, with no information available on its purity.

B. Single-Emitter Characterization

To interpret data recorded for the full emitter array, it is informative to know the emission characteristics of a single-emitter tip of such arrays. In this study, all emitter tips of an existing emitter array were mechanically removed, except one emitter located in the center of the glass chip. This way, the emission behavior of a single tip could be studied while maintaining the same alignment and packaging features of the full thruster, thus allowing for direct comparison. Due to the significantly decreased propellant consumption when compared to the full array, no dedicated propellant tank was necessary, as discussed in Sec. IV.A.

Figure 4 shows the current emitted from a single-emitter tip as a function of applied voltage. The distinct current step associated with the onset of the main emission site, followed by a moderate increase of the current emitted by this emission site with increasing potential, is easily identifiable and was independently confirmed in [28] by spatial scanning of the emission sites. The onset current for this emission site is found to be ~500 nA. With increasing electrical

**Data available online at ary https://gameon.nasa.gov/files/2015/11/FS-MEP_factsheet_130124.pdf [retrieved 03 January 2016].

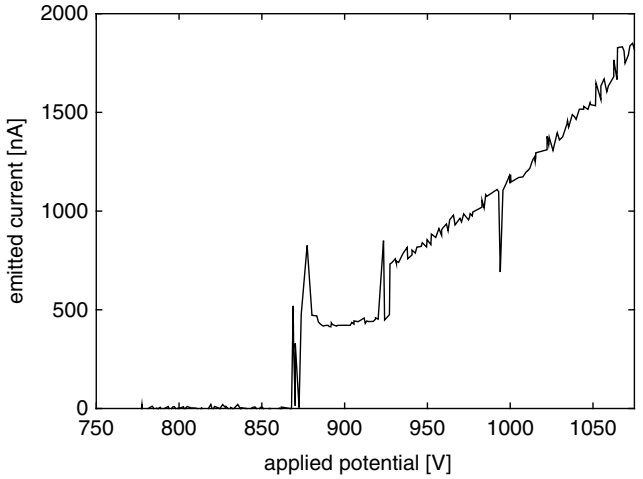

Fig. 4 Emitted current as a function of applied emitter potential showing discrete steps indicating the onset of a new emission site.

stressing, the onset of a secondary emission site is clearly noticeable at ∼925 V, followed again by a continuous increase in current for increasing emitter potential. Angular divergence and energy-resolving measurements were first conducted at an emission current of $I_{em} = 500$ nA. The emission potential was then further increased until a second step in emission current was noticed, indicating the onset and establishment of a secondary emission site. Again, angular divergence measurement and energy-resolving measurements were performed at this emission condition.

Figure 5 shows the angular beam distribution for the single emitter corresponding to the two investigated emission currents. The first key finding in these data is that the first emission site is not located centrally, which would constitute the point of highest electric field in an ideal emitter. This is most likely caused by blockage of the emitter apex or tip irregularities, given the fact that the tips' radii of curvatures are on the order of magnitude as the largest particle sizes found in the porous glass.

The second finding is that the increased stressing due to potential increase (up to a point where a new emission site is opened up) did not significantly change the shape and location of the main emission site.

The third important finding is that the secondary emission site is located almost exactly mirrored to the first emission position, further suggesting blockage of the emitter apex and making it inaccessible to liquid, thus making a surface around the apex the most favorable location for emission. It should be noted that, although the angular scan is only capable of capturing the beam in a single plane, monitoring the emission current indicates that no additional emission sites are present when conducting this study. However, because the setup does not ensure that the sensor passes through equal parts of the

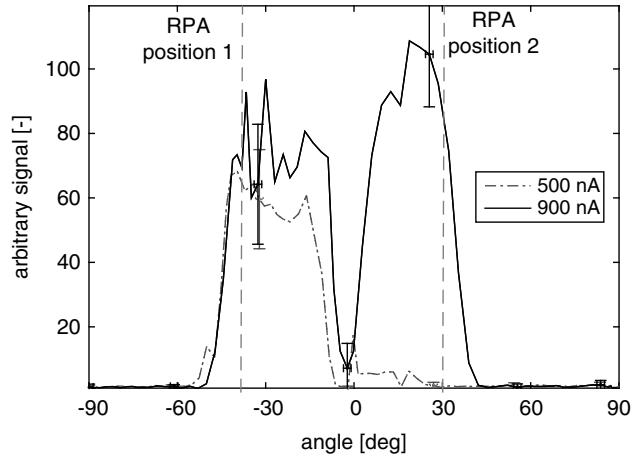

Fig. 5 Angular beam divergence data for single emitter in positive emission polarity showing one and two emission sites; dashed lines indicate positions of RPA measurements.

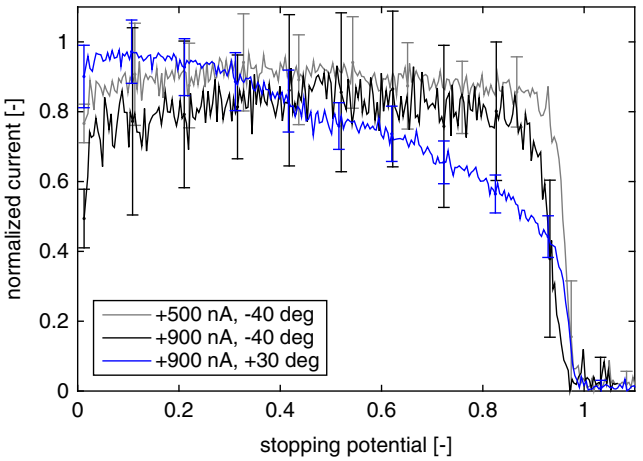

Fig. 6 RPA data for single emission site and two emission sites, taken at the indicated positions.

beamlets, the recorded data do not allow conclusions regarding the relative intensity of the beamlets. This experiment is repeated in positive emission polarity with similar results.

After stopping and restarting emission repeatedly to show stability of position of the emitted beams, RPA measurements were performed at different locations (−40 and +30 deg) corresponding to the two individual beams. This was done for different emission current levels, corresponding to the presence of one ($I_{em} = 500$ nA) and two beams ($I_{em} = 900$ nA). The resulting, normalized, RPA data are shown in Fig. 6.

The first key finding of this is that the main emission site indicates a very narrow energy distribution close to the emission potential and only little indications of particle breakup events, in which solvated ions break up into a neutral and a lighter ion at some point during or after acceleration [29,30]. Second, a comparison of the RPA data recorded for the main emission site at low current levels ($I_{em} = 500$ nA) to the scan performed in the presence of the secondary emission site ($I_{em} = 900$ nA) shows that the energy composition of the main emission site does not change significantly, despite the increased electrical stressing. However, the RPA data corresponding to the secondary emission site (+30 deg) show a largely different distribution, with the energy population distributed to values significantly smaller than the emission potential. The possible presence of emission sites with significantly altered energy properties on the same individual emitter will later explain the broad energy spread found for the full emitter array, indicating that the energy distribution broadening is not originating from stressed emission sites but from emergence of additional emission sites that are emitting under largely different conditions, and therefore lead to different energy distribution of the emitted particles.

C. Full-Array Characterization

1. *I(V) Curves*

Figure 7 shows the emitted and intercepted currents as a function of applied emitter potential. At an emission current of ±150 μA, the relative interception, which is the ratio of current intercepted by the extractor electrode to total emitted current, is 4.8–5.5%.

Figure 8 compares emitted currents as a function of applied potential for different ionic liquids. For constant emitter potentials, the highest emission currents are found for EMI–$GaCl_4$, followed by EMI-DCA, due to the difference in stressing condition and flow properties.

2. *RPA Measurements*

Figure 9 shows RPA data recorded at positive and negative emission currents of $I_{em} = \pm 150$ μA for the three different ionic liquids. All RPA data show significant energy spreading. This is consistent with the energy-resolving results obtained for single emitters (Fig. 6), which indicates the presence of emission sites with different energy properties.

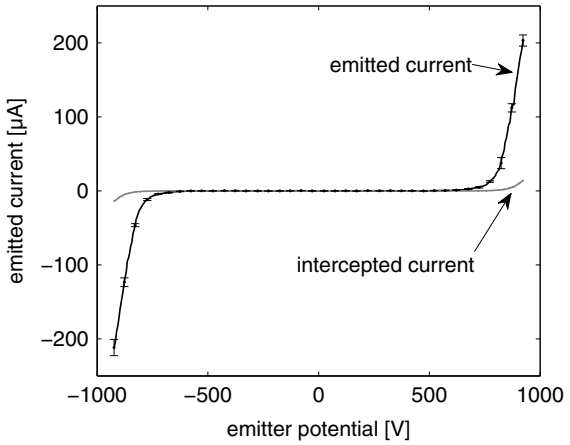

Fig. 7 Emitted and intercepted current as function of applied potential for EMI–BF_4.

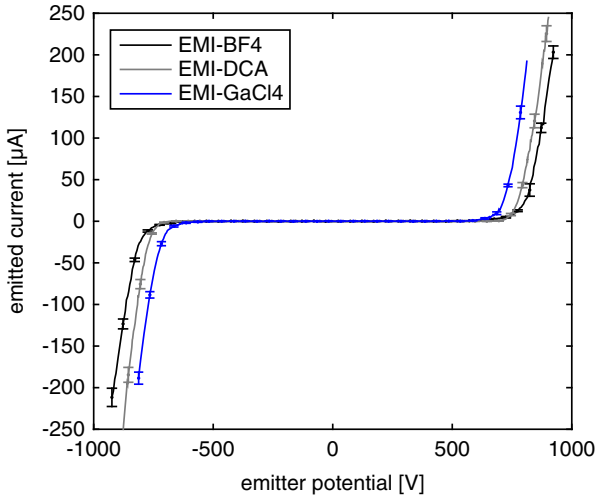

Fig. 8 Emitted currents as a function of applied potential for different ionic liquids.

Comparing the RPA data of different propellants shows increased amount of particles with lower energies, perhaps due to fragmentation, for EMI–BF_4 and, to a lesser extent, for EMI-DCA as compared to EMI–$GaCl_4$.

3. *Spatial Beam Distribution Measurements*

Figure 10 shows the beam divergence of the full emitter array measured in both polarities for different ionic liquids. Misalignment of the thrust vector, defined as the centroid of the recorded beam distribution, and the zero axis of the measurement is caused by alignment inaccuracy of the thruster with the measurement axis upon mounting.

All three measurements show good agreement of spatial emission for alternate polarities and symmetric plume shapes. A larger beam opening angle is noticed for the full beam when compared to previously reported results for single emitters [16]. Comparison to the results presented on the spatial distribution of beamlets of individual porous glass emitter tips presented in Sec. IV.B suggests that the increased beam spreading for the full array is caused by superposition of multiple offaxis emitted beamlets.

Comparing the spatial distributions for different propellants shows that, although all feature the same maximum opening angle of an approximately 60–70 deg half-angle, the full width at half-maximum is smaller for EMI-DCA as compared to EMI–BF_4, and it decreases further for EMI–$GaCl_4$. A detailed discussion of these results is given in Sec. V.

4. *Time-of-Flight Measurements*

Figure 11 shows the time of flight recorded for EMI–BF_4 at different emission current levels for both polarities, assuming singly charged particles. The masses corresponding to the ions with solvation degree n, assuming singly charged species emitted at applied potentials (a simplification, given the width of the energy distributions), are indicated by dashed lines. Fragmentation events occurring in the beam lead to broadening of the energy distribution of the particles (Fig. 9), partially obscuring the distinct current steps expected for individual beam species [31]. The recorded data clearly show a prevailing population of monomers and dimers (single and singly solvated ions) in both polarities, with a smaller content of higher-order solvated ions. In addition, a population of significantly lower specific charge, which are presumably charged droplets, is noticeable in both polarities. It is interesting to notice that the composition does not vary within the emission current, indicating the specific impulse to be solely dependent on the square root of the emitter potential in this regime.

5. *Extended Test Behavior*

Figure 12 shows the time traces of the emitted and intercepted currents, as well as the applied emitter potential for a long-duration test of 85 h using a polarity alternation period of 30 s. Occasional rapid current overshoots in emitted and intercepted signals correlate with discharge events. In this test, the emitter potential is kept constant throughout the test, and the test duration is chosen until a noticeable decay in emitted current is observed, which is after approximately 85 h. The current traces recorded exceeding a firing time of 85 h indicate that the propellant flow may become partially interrupted, but more work is required to understand the causes of this propellant decay.

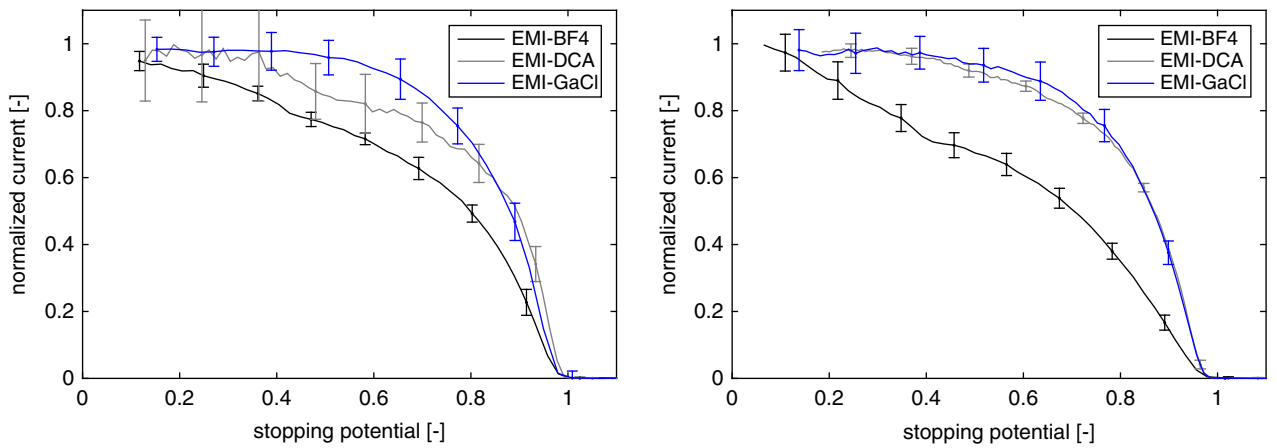

a) Positive emission mode **b) Negative emission mode**

Fig. 9 RPA data recorded for different ionic liquids.

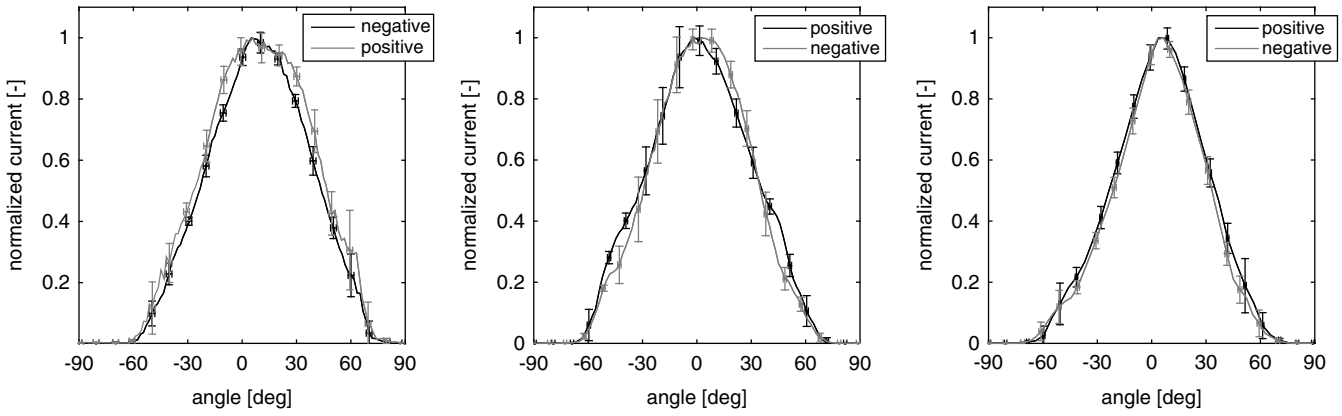

a) EMI-BF4 **b) EMI-DCA** **c) EMI-$GaCl_4$**

Fig. 10 Angular beam divergence at $i = 150\ \mu$A for different propellants.

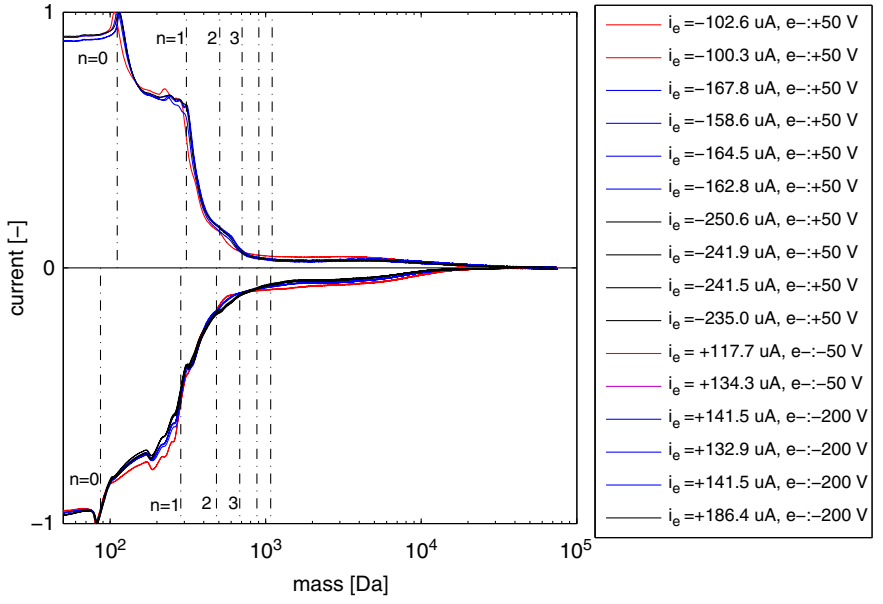

Fig. 11 Time-of-flight data for $EMI{-}BF_4$ at different emission currents (Da, Dalton).

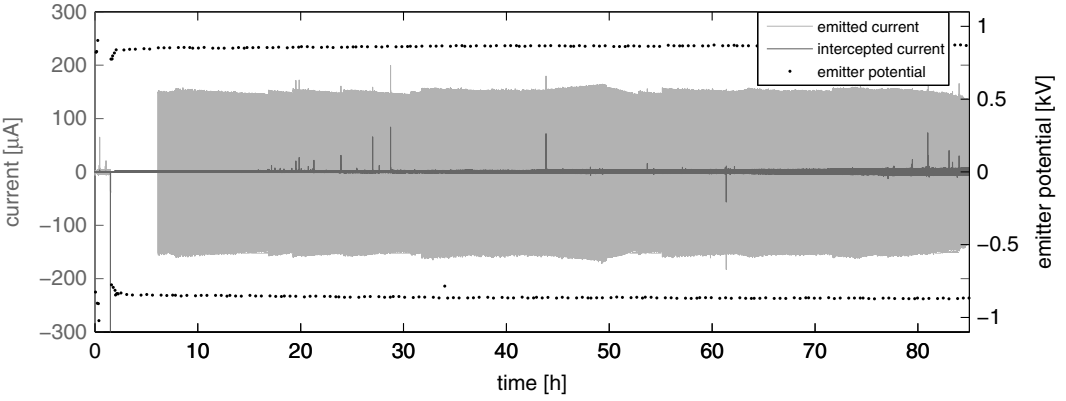

Fig. 12 Emitted and intercepted current, together with applied emitter potential during a 85 h test.

A clear trend of increasing relative interception was noticed over the duration of the entire test, ranging from less than 2–8%. Inspection of emitters after different firing times shows the formation of "bridges" of what appears to be decomposed ionic liquid linking individual emitters to the extractor, as shown in Fig. 13. These bridges are anticipated to be the result of discharges, which could allow small leakage currents and contribute to an increase in the intercepted current as their number increases over time. Over the test duration shown in Fig. 12, 0.5954 g of propellant were consumed. The average charge-to-mass ratio of the emitted beam was determined as $q/m = 72.5$ C/g.

Ensuring a constant propellant supply, the specific impulse for an ideal loss-free thruster can be estimated as

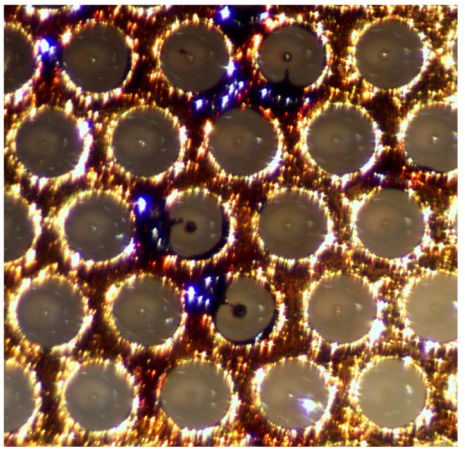

Fig. 13 Decomposed ionic liquid bridging individual emitters to the extractor after long firing durations.

$$I_{\mathrm{sp}}^{\mathrm{ideal}} = \frac{1}{g_0}\sqrt{2V_e\frac{q}{m}} \tag{1}$$

and is summarized in Table 1 for several thrusters. To exclude uncertainties in the determination of specific impulse originating from varying potentials, each of these tests was stopped as soon as a decrease in emission current was noticed unless otherwise noted. Determining the propellant mass consumed during this duration allowed us to estimate the specific impulse for constant low-emission potential, as summarized in Table 1.

For emitters RG230 and RG107, tests were conducted exceeding the onset of emission current decay (beyond 70–85 h into the test) caused by decreasing propellant feed flow. To maintain emission current in these tests, the emission potential was increased during these tests once current decay was observed in the measured emission current data [25], and it was manually adjusted to maintain an average emission current of $I \sim 150\ \mu$A. It is expected that, at this stage of decreasing propellant supply and increased electrical stressing, the liquid distribution in the emitter and the emitter surface changed, effectively changing the charge-to-mass ratio of the emitted beam. This ultimately led to correspondingly higher average specific impulse for these tests, as indicated in Table 1. It is worth noting that, although later results from time-of-flight experiments indicated constant q/m for a variety of emitter potentials, these results showed that a change in propellant feed flow, and therefore liquid distribution in the emitter, can impact q/m. The longest lifetime found in a single test was 172 h [25]. This test consumed 0.6306 g of propellant, with an average specific charge of $q/m = 125$ C/g. This led to an overestimation of I_{sp} in the early operational phase and a corresponding underestimation for the final part of the test, given the increase in emission potential necessary to maintain the emission current level of $I_{\mathrm{em}} = 150\ \mu$A.

6. *Thrust Measurement*

Thrust measurements were performed on individual thrusters and pairs of thrusters operated with EMI–BF_4 as propellant. Two independent measurements, as described in Sec. III, were used to measure thrust on two identical thrusters each. Thrusters were characterized as firing in parallel in the magnetically levitated balance setup at Massachusetts Institute of Technology (MIT) and in parallel sessions using the NASA John H. Glenn Research Center (GRC) balance. A comparison of the recorded thrust data as a function of emitted current is shown in Fig. 14.

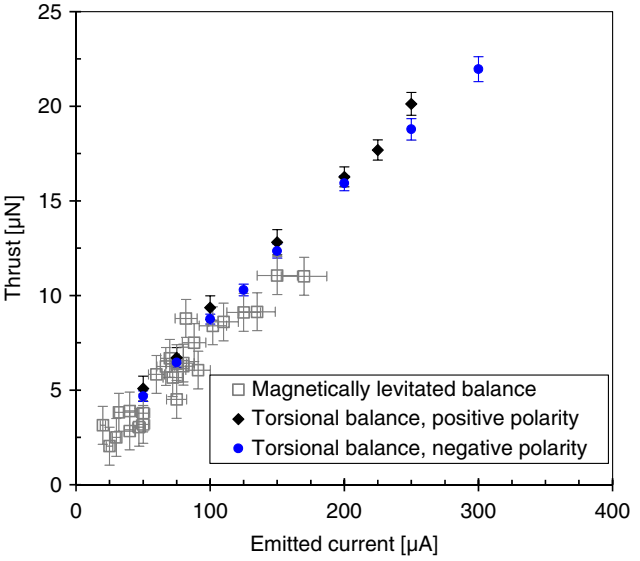

Fig. 14 Thrust as a function of emission current for two independent measurements performed at NASA GRC and MIT.

Both measurements were able to confirm the expected linear dependency of thrust with emitted current [32] and showed good correspondence with each other, within the spread of data uncertainty. A detailed discussion of the results, and cross correlation to other characterization results, can be found in Sec. V.

V. Discussion and Analysis

A. Specific Impulse

1. *Indirect Estimation of Specific Impulse*

The mass resolving information and the relative intensity of the different species contained in the time-of-flight data allow us to determine the specific impulse corresponding to the emitted particle beam, according to [2,33]

$$I_{\mathrm{sp}} = \frac{T}{g_0\dot{m}} \tag{2}$$

where g_0 is the standard acceleration due to gravity, and the thrust and mass flow are calculated from the time-of-flight data. The thrust T_{ToF} and mass flow $\dot{m}_{\mathrm{ToF}}$ are calculated according to [15]

$$T_{\mathrm{ToF}} = -\frac{2|V_e|}{L}\int_0^\infty t\frac{\mathrm{d}I}{\mathrm{d}t}\,\mathrm{d}t \tag{3}$$

$$\dot{m}_{\mathrm{ToF}} = -\frac{2V_e}{L^2}\int_0^\infty t^2\frac{\mathrm{d}I}{\mathrm{d}t}\,\mathrm{d}t \tag{4}$$

Table 1 Long-duration test data

Thruster label	q/m, C/g	$I_{\mathrm{sp}}^{\mathrm{ideal}}$, s	Emitter potential, V	Test duration, h	Propellant
RG83	76.3	1156 ± 75	~855	74	0.3846
RG108	72.0	1194 ± 79	~907	60	0.3599
RG183	72.1	1173 ± 79	~850	60	0.4023
RG286	72.5	1147 ± 77	~860	92	0.5954
Tests including manual increase of emitter potential					
RG230	82.7	1303	~870–1460	126	0.6057
RG107	126.0	1717	~835–1480	172	0.6306

where L is the potential free drift distance between electrostatic gate and detector; V_e is the emission potential; and $\mathrm{d}I/\mathrm{d}t$ is the derivation of the time-of-flight signal current in time, normalized by the surface integral.

Fragmentation upstream of the extractor electrode leads to ions with faster velocities compared to the unfragmented ion, but slower compared to nonsolvated ions of the same species [31], and is therefore expected to lead to a slight overestimation of the specific impulse when derived from Eqs. (3) and (4). In the experiments presented in Sec. IV.C.4, the extractor grid was biased to the opposite polarity of the emitter to enhance the stopping effect of the electrostatic gate. Because the gate grid is pulled to ground in the open state, the particle beam experiences a net deceleration before entering into the field free drift region between the gate and the collector. To account for this effect, the specific impulse is corrected by the square root of the ratio of applied potentials to calculate the true specific impulse according to

$$I_{\mathrm{sp}}^{\mathrm{true}} = I_{\mathrm{sp}}\sqrt{\frac{V_e - V_{\mathrm{ex}}}{V_e}} \tag{5}$$

where V_e and V_{ex} are the emitter and extractor potentials, respectively. As this method is highly sensible to measurement noise in the recorded data long after the measured signal decays to zero [time appears squared within the expression for $\dot{m}$ in Eq. (4)], it has been suggested to use an exponential fit in the trailing edge of the droplet signal [34]. This allows us to extend the integrals over the entire measurement range without introducing errors due to measurement artifacts. This approach has been used to calculate specific impulse from the data presented in Fig. 11. It can then be argued that, due to the importance of high mass species, the largest uncertainty is introduced by applying this exponential fit in the droplet signal's trailing edge. Uncertainty in this determination can therefore be estimated as the difference in I_{sp} data calculated using the exponential fit and the measured raw data. Figure 15 plots the calculated specific impulse based on time-of-flight measurements with corresponding uncertainties. In addition, the time-of-flight data are used to estimate the thrust. However, because effects such as the angular beam spreading are not incorporated in this analysis, significant overestimation of the thrust occurs for data based solely on time-of-flight measurements as compared to the direct thrust measurements in Fig. 14.

The derived specific impulse at an emission current of $I_{\mathrm{em}} = 150 \pm 50\ \mu$A is calculated as $I_{\mathrm{sp}}^{+} = 1035.5 \pm 52$ s with a measurement accuracy of ± 345 s for positive polarity and $I_{\mathrm{sp}}^{-} = 1062.1 \pm 70$ s with a measurement accuracy of ± 298 s for negative emission polarity.

These specific impulse data can be confirmed in independent measurements by determining the propellant mass consumption in long-duration tests, in conjunction with the integrated net emitted current, as presented in Sec. IV.C.5. Averaging over multiple tests presented in Table 1 yields the specific impulse for constant emitter potential of $I_{\mathrm{sp}}^{\mathrm{ideal}} = 1167 \pm 21$ s with a measurement accuracy of ± 79 s. This is in good agreement with the specific impulse values determined via the time-of-flight analysis. However, both indirectly calculated specific impulse values do not incorporate emission inefficiencies, most prominently due to angular beam spreading, as discussed hereafter.

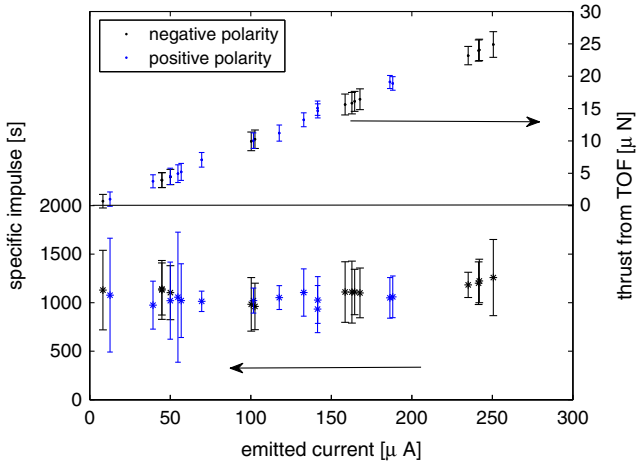

Fig. 15 Specific impulse and thrust from time-of-flight experiments. Angular effects are not considered for thrust calculation.

2. *Direct Calculation of Specific Impulse*

Both ways of calculating the specific impulse indirectly based on time-of-flight and current measurements discussed in Sec. V.A.1 do not take efficiencies that are discussed in Sec. V.B into account. For example, the angular distribution of accelerated particles reduces the effective axial velocity of particles, which are either not captured by the time-of-flight detector due to geometrical constraints or which are not accounted for when calculating the average charge-to-mass ratio according to Eq. (1). The true specific impulse can be calculated by using thrust data presented in Sec. IV.C.6 and propellant mass flow determined by data provided in Sec. IV.C.5 according to

$$I_{\mathrm{sp}} = \frac{T}{\dot{m} g_0} \tag{6}$$

It should be noted that thrust data and data used to determine the propellant consumption are based on separate measurements of identical thruster designs. According to the data on fire duration and total propellant consumption by mass loss in Table 1, the average propellant mass flow corresponding to an emission current of $I_{\mathrm{em}} = 150\ \mu$A can be calculated as $\dot{m}_{150\mu A} = 1.69 \pm 0.19 \cdot 10^{-9}$ kg/s. The corresponding thrust from Fig. 14 (GRC data) is $T = 12.6 \pm 0.7\ \mu$N, leading to a specific impulse of $I_{\mathrm{sp}} = 758.9 \pm 40.7$ s. Comparison to the indirectly determined specific impulse values from extended duration firings in Sec. V.A.1 shows that the decrease aligns well with the decrease expected from inefficiencies due to nonaxial acceleration of the beam, energy inefficiencies, and polydispersive efficiencies as discussed in Sec. V.B. However, it should be noted that the specific impulse derived using time-of-flight would overestimate these values, when incorporating angular and energy efficiency, by approximately 10%.

B. Thruster Efficiency

1. *Thruster Efficiency Components*

Emitters have been characterized using a standard procedure of scanning the applied emitter potential while recording the emitted and intercepted currents. The emission characteristics of three different ionic liquids have been studied in identical emitter configurations, showing increased emission current of propellants EMI-DCA and EMI–$GaCl_4$ as compared to EMI–BF_4. Table 2 summarizes physical parameters for these propellants [35]. Assuming Darcy's law [36], the propellant flow rate is inversely proportional to the hydraulic impedance, and thus the viscosity. For constant emitter potential, assuming similar droplet compositions, the highest emission currents would be expected for the ionic liquid with the smallest viscosity (EMI–$GaCl_4$) and the smallest currents for EMI–BF_4, given the similar surface tensions of the liquids tested. However, additional time-of-flight data would be necessary to confirm this dependency. In addition to comparison of emission characteristics of different propellants, the transmission efficiency, defined as the ratio of net emitted current to the total current drawn from the emitter, was calculated using data recorded in scans of current as a function of applied voltage I(V) scans. At an emission current of $I_{\mathrm{em}} = 150\ \mu$A, for the propellant EMI–BF_4, the transmission efficiency, defined as the ratio of current passing the extractor without being intercepted to the total emitted current, is determined as $\eta_{\mathrm{tr}}^{+} = 0.981 \pm 0.006$ and $\eta_{\mathrm{tr}}^{-} = 0.982 \pm 0.011$ for positive and negative emission polarities, respectively.

The spatial distribution measurements on individual emission beamlets presented in Sec. IV.B show half-opening angles of ~20 deg for both main and secondary emission sites, which is in

Table 2 Physical properties of ionic liquids at 25°C, unless otherwise noted [35]

Ionic liquid	Density, g/cm^3	Conductivity, S/m (Siemens/meter)	Viscosity, 10^{-3} Pa (Millipascall)	Surface tension, 10^{-3} N/M	±Ion mass, Da (Dalton)
EMI–BF_4	1.28	1.4	37	45.2	111.2/86.8
EMI–DCA	1.08	2.8	21	49.05	111.2/66
EMI–$GaCl_4$	1.53	2.0	13	48.6	111.2/211.5

agreement with previously reported opening angles for single-emitter beams [16]. However, the spatial beam distribution results for single emitters presented in Sec. IV.B also indicate that individual beamlets can be emitted offaxis. Because space charge and collision effects are expected to be negligible given the charge densities involved, it could be assumed that the increased angular distribution for the full emitter array is the result of a superposition of multiple narrow, offaxis emission beamlets.

Comparison of opening angles of different propellants shows that, although different liquids have different full width at half maximum, their total spread is similar, and it is most likely associated to the inability of many tips to emit onaxis.

Knowledge of the spatial beam distribution can be used to determine an angular efficiency defined as the ratio of the velocity component of the accelerated particles parallel to the main thrust axis and the overall velocity of accelerated particles, according to [37]

$$\eta_\Phi = \int_0^{\Phi_0} f(\Phi)\cos\Phi \, \mathrm{d}\Phi^2 \tag{7}$$

where $f(\Phi)$ is the current distribution function over angle Φ. The axisymmetric nature of the emitted beam invoked by this expression is justified by the symmetric shape of the beam along one axis in Fig. 10. Because data were recorded over ±180 deg, the central thrust angle was determined as the angle at which the integrals over the distributions become equal to both sides. Equation (7) was then used to calculate left-handed and right-handed efficiencies of the normalized data. Subsequently, an averaged efficiency was calculated, incorporating an error propagation calculation. Approximating the emitter as a point source, which is neglecting the finite source size, the angular efficiency for EMI–BF_4 was determined as $\eta_\Phi^+ = 0.801 \pm 0.055$ and $\eta_\Phi^- = 0.828 \pm 0.045$ for positive and negative emission polarities, respectively.

The combined data presented in Sec. IV on single emitters and full arrays allows us to draw multiple conclusions on the energetic state of emission in this version of ionic liquid electrospray array thrusters. The investigation of the emission of a single emitter in Sec. IV.B shows the possibility of coexistence of multiple stable emission sites per emitter tip, operating in different energetic emission regimes. The data presented show that an emission site emitting particles with a narrow energy distribution close to the emitter potential is not disturbed by the onset of a secondary emission site but, instead, maintains its location and energetic emission properties. The energy properties of the secondary emission site are found to widely differ from the main emission site, showing a broader energy distribution with significantly lower energies, including indications of fragmentation events. This shows that emission properties likely depend on the structure of individual emission sites, and the existence of multiple emission sites per tip does not necessarily always result in a decrease in performance. Throughout testing, energetic and spatial properties of both emission sites are found repeatable. Given the proximity of the emission sites, no difference in propellant supply other than local pore size is anticipated, and the different energy spectrum is attributed to a less favorable location of the secondary emission site in terms of surface structure, such as increased pore size with different liquid accumulation state on the surface. Given existing nonuniformities in propellant distribution across the emitter array due to a central, finite area propellant supply, a nonuniform distribution of emission currents across the emitter array is anticipated, facilitating regions of emitters with multiple emission sites per emitter. The emitted beam of the full thruster array is therefore considered a superposition of individual emission beamlets featuring significantly different energy properties. Such a superposition explains the large energy spread found in the energy distribution recorded for full thruster arrays in Sec. IV.C.

The energy resolving data allow us to derive an energy efficiency, defined as the ratio of effective beam acceleration potential V_B to the applied emitter potential V_e. Attributing low-voltage signals to processes occurring past emission, the effective beam acceleration potential V_B is given by the voltage corresponding to the maximum of the premier peak in the ion energy distribution function. The ion energy distribution function is calculated by taking the first derivative of the measured RPA signal as a function of voltage [37–39]:

$$\eta_E = \frac{V_B}{V_e} \tag{8}$$

For propellant EMI–BF_4, averaging over multiple emitter arrays, the energy efficiency becomes $\eta_E^+ = 0.906 \pm 0.067$ and $\eta_E^- = 0.931 \pm 0.036$ for positive and negative emission polarities, respectively.

The data recorded from the time-of-flight experiment in Fig. 11 can be used to derive the polydispersive efficiency [40] according to

$$\eta_p = \frac{T_{\mathrm{ToF}}^2/2\dot{m}_{\mathrm{ToF}}}{V_e I_{\mathrm{em}}} \tag{9}$$

where V_e and I_{em} refer to the applied emitter potential and the total emitted current, respectively. By taking data from the time-of-flight experiment only in these calculations, no influence from beam spreading or energy deficiency is found in Eq. (9), hence yielding the polydispersive efficiency. The thrust T_{ToF} and mass flow $\dot{m}_{\mathrm{ToF}}$ are calculated using Eqs. (3) and (4), applying the same approximation for the trailing droplet edge as discussed in Sec. V.A.1. The polydispersive efficiency determined by averaging over all tests presented in Fig. 11 is calculated as $\eta_p^+ = 0.5323 \pm 0.0122$ and $\eta_p^- = 0.5545 \pm 0.0260$ for positive and negative emission polarities, respectively. The large efficiency losses due to the presence of droplets in the emitted beam points to the importance of reducing the emitted droplet population in future emitter designs.

The total thruster efficiency can be calculated according to [37]

$$\eta_{\mathrm{total}} = \eta_i \eta_{\mathrm{tr}}^2 \eta_\Phi \eta_E \eta_p \tag{10}$$

with η_i being the ionization efficiency, taken as unity because no direct evaporation of neutrals is observed in ionic liquids; η_{tr} is transmission efficiency; η_Φ is the angular efficiency; η_E is the energy efficiency; and η_p is the polydispersive efficiency, which were all discussed earlier in this section. Including error propagation analysis, the total thruster efficiency is then approximated as $\eta_{\mathrm{total}}^+ = 0.379 \pm 0.062$ and $\eta_{\mathrm{total}}^- = 0.42 \pm 0.068$ for positive and negative emission polarities, respectively. It is noted that the major factor impacting this efficiency is due to the polydispersive efficiency caused by the presence of droplets in the emitted ion beam.

2. *Direct Calculation of Thruster Efficiency*

The total thruster efficiency can be calculated according to

$$\eta_{\mathrm{total}} = \frac{T^2/2\dot{m}}{V_e I_{\mathrm{em}}} \tag{11}$$

using the directly measured thrust (Sec. IV.C.6) and the mass flow determined by propellant consumption (Sec. IV.C.5), in conjunction with the directly measured applied emitter voltage V_e and emitted current I_{em}. Using the same parameters as in Sec. V.A.2

for mass flow of $\dot{m}_{150\,\mu A} = 1.69 \pm 0.19 \cdot 10^{-9}$ kg/s and thrust of $T = 12.6 \pm 0.7$ μN, at an emission current of $I_{em} = 150$ μA, the directly calculated thruster efficiency, averaged over both emission polarities, becomes $\eta_{total} = 0.361 \pm 0.081$.

C. Extended Duration Testing

Firing tests over long durations at polarity alternation intervals of 30 s show a stable emission current for typically 40–80 h before current decay is observed. This decay in current has been traced back to inadequate propellant supply from the propellant reservoir rather than processes occurring in the emitter itself. Over the lifetime, a steady increase in intercepted current for typically less than 2% to ~10% of the emitted current is observed. The maximum lifetime of the porous glass MEMS emitter thruster in these experiments, fired at an average design emission current of 150 μA, is found to be 172 h before a short between the emitter array and the extractor terminates the test. It is found that propellant accumulation on the emitter tip and discharges induced by this accumulation caused this short.

D. Thrust

Two independent thrust measurements have been conducted, employing different measurement principles. Measurements taken on the different experimental setups corresponded sufficiently well with each other, with larger measurement uncertainties on the magnetically levitated balance. It should be pointed out that, although the torsional thrust balance was able to resolve thrust measurements according to different polarities, the nature of the magnetically levitated thrust balance necessitated firing a pair of thrusters in opposite polarity, and the thrust derived was therefore an average over polarities. In addition, deriving thrust by a change of rotational motion of the levitated structure also led to thrust measurements averaging over each test duration of approximately 20 min. The thrust data recorded for the torsional thrust balance, on the other hand, showed smaller measurement uncertainties and reduced standard deviation over repeated tests, as well as the linear behavior of thrust as a function of emission current up to high emission currents.

Direct measured thrust using the torsional thrust balance is compared in Fig. 16 to indirectly determined thrust using time-of-flight data by Eq. (3), modified according to the angular and energy efficiency calculated in Sec. V.B.1. Data from the levitational balance are omitted in this comparison to avoid cluttering of the plot. Interpolating values to the nominal current of 150 μA, this indirectly determined thrust yields an overestimation of approximately 10%, which is within the error bars.

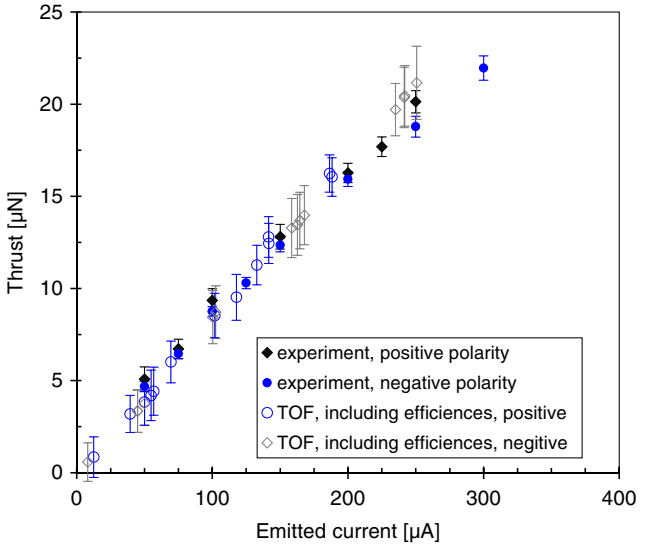

Fig. 16 Comparison of direct thrust measurements (GRC balance) to thrust derived from time-of-flight experiments, incorporating independently derived thruster efficiency.

VI. Conclusions

A full characterization of microelectromechanical systems-based ionic liquid electrospray thrusters is presented, including two independent measurements of thrust of $T \sim 11$–12.5 μN at an emission current of $I_{em} \sim 150$ μA for a ~1 cm^2 device. The ideal specific impulse without angular beam divergence and energy losses is independently determined using time-of-flight measurements and extended duration testing, yielding $I_{sp}^{ideal} \sim 1050$–1150 s. In addition, the specific impulse is directly calculated based on thrust measurements and the propellant mass flow rate determined by extended duration firings, therefore including all thruster inefficiencies and leading to a specific impulse of $I_{sp} \sim 760$ s. This decrease in actual specific impulse corresponds well to independently determined inefficiencies due to nonaxial particle acceleration, energy inefficiencies, and polydispersive efficiency.

A characterization of individual thruster efficiency contributions is presented, including transmission efficiency, angular efficiency, energy efficiency, and polydispersive efficiency. The total thruster efficiency is calculated as $\eta_{total} \sim 36\%$. A detailed discussion of individual efficiency components shows, among others, transmission efficiencies greater than 98% but significant losses due to angular beam spreading and the polydispersive nature of the emitted beam. Although single ions and singly solvated ions are found to be the dominant species in the emitted beam, the emitters are found to operate in a mixed ion-droplet operation mode. The presence of droplets in the emitted ion beam is identified as the major cause for reduced efficiency, and it highlights the importance of reduction of emitted droplets in future electrospray emitter designs.

Finally, the emission behavior during extended firings is presented, showing stable emission up to ~90 h, before propellant feed flow decays, necessitating an increase of the applied emitter potential to sustain a nominal current level of 150 μA. This characterization serves to define the fundamental operational properties of this type of propulsion system and will be useful in guiding the design of future implementations.

Acknowledgments

This work was supported by NASA through contract no. NNL13AA12C under NASA's Game Changing Development program of the Space Technology Mission Directorate. The authors would like to thank Corey Fucetola and Alex Bost for their contributions in the fabrication of the electrospray thrusters and Catherine Miller for synthesizing the 1-Ethyl-3-Methylimidazolium Tetrachlorogallate.

References

[1] Selva, D., and Krejci, D., "A Survey and Assessment of the Capabilities of Cubesats for Earth Observation," *Acta Astronautica*, Vol. 74, May–June 2012, pp. 50–68. doi:10.1016/j.actaastro.2011.12.014

[2] Gamero-Castano, J., and Hruby, V., "Electrospray as a Source of Nanoparticles for Efficient Colloid Thrusters," *Journal of Propulsion and Power*, Vol. 17, No. 5, 2001, pp. 977–987. doi:10.2514/2.5858

[3] Carretero Benignos, J., "Numerical Simulation of a Single Emitter Colloid Thruster in Pure Droplet Cone-Jet Mode," Ph.D. Dissertation, Massachusetts Inst. of Technology, Cambridge, MA, 2005.

[4] Martinez-Sanchez, M., de la Mora, J. F., Hruby, V., Gamero-Castano, M., and Khayms, V., "Research on Colloid Thrusters," *26th International Electric Propulsion Conference*, IEPC Paper 99-014, Electric Rocket Propulsion Soc., Fairview Park, OH, 1999.

[5] Lozano, P., and Martinez-Sanchez, M., "Experimental Measurements of Colloid Thruster Plumes in the Ion-Droplet Mixed Regime," *38th AIAA/ASME/SAE/ASEE Joint Propulsion Conference and Exhibit*, AIAA Paper 2002-3814, 2002.

[6] Lozano, P., and Martnez-Sánchez, M., "Ionic Liquid Ion Sources: Suppression of Electrochemical Reactions Using Voltage Alternation," *Journal of Colloid and Interface Science*, Vol. 280, No. 1, 2004, pp. 149–154. doi:10.1016/j.jcis.2004.07.037

[7] Zaitsau, D. H., Kabo, G. J., Strechan, A. A., Paulechka, Y. U., Tschersich, A., Verevkin, S. P., and Heintz, A., "Experimental Vapor

Pressures of 1-Alkyl-3-Methylimidazolium Bis(trifluoromethylsulfonyl)Imides and a Correlation Scheme for Estimation of Vaporization Enthalpies of Ionic Liquids," *Journal of Physical Chemistry A*, Vol. 110, No. 22, 2006, pp. 7303–7306. doi:10.1021/jp060896f

[8] Spindt, C., "Microfabricated Field-Emission and Field-Ionization Sources," *Surface Science*, Vol. 266, Nos. 1–3, 1992, pp. 145–154. doi:10.1016/0039-6028(92)91012-Z

[9] Pranajaya, F., and Cappelli, M., "Development of a Colloid Micro-Thruster for Flight Demonstration on the Emerald Nanosatellite," *37th Joint Propulsion Conference and Exhibit*, AIAA Paper 2001-3330, 2001.

[10] Krpoun, R., and Shea, H. R., "Integrated Out-of-Plane Nanoelectrospray Thruster Arrays for Spacecraft Propulsion," *Journal of Micromechanics and Microengineering*, Vol. 19, No. 4, 2009, Paper 045019. doi:10.1088/0960-1317/19/4/045019

[11] Gassend, B., "A Fully Microfabricated Two-Dimensional Electrospray Array with Applications to Space Propulsion," Ph.D. Dissertation, Massachusetts Inst. of Technology, Cambridge, MA, 2007.

[12] Courtney, D. G., Li, H. Q., and Lozano, P., "Emission Measurements from Planar Arrays of Porous Ionic Liquid Ion Sources," *Journal of Physics D: Applied Physics*, Vol. 45, No. 48, 2012, Paper 485203. doi:10.1088/0022-3727/45/48/485203

[13] Tang, K., Lin, Y., Matson, D. W., Kim, T., and Smith, R. D., "Generation of Multiple Electrosprays Using Microfabricated Emitter Arrays for Improved Mass Spectrometric Sensitivity," *Analytical Chemistry*, Vol. 73, No. 8, 2001, pp. 1658–1663. doi:10.1021/ac001191r

[14] Arscott, S., Le Gac, S., Druon, C., Tabourier, P., and Rolando, C., "Micromachined 2D Nanoelectrospray Emitter [Mass Spectrometer Applications]," *Electronics Letters*, Vol. 39, No. 24, Nov. 2003, pp. 1702–1703. doi:10.1049/el:20031099

[15] Courtney, D. G., Dandavino, S., and Shea, H., "Comparing Direct and Indirect Thruster Measurements from Passively Fed and Highly Ionic Electrospray Thrusters," *Journal of Propulsion and Power*, Vol. 32, No. 2, 2016, pp. 392–407. doi:10.2514/1.B35836

[16] Lozano, P., and Martnez-Sánchez, M., "Ionic Liquid Ion Sources: Characterization of Externally Wetted Emitters," *Journal of Colloid and Interface Science*, Vol. 282, No. 2, 2005, pp. 415–421. doi:10.1016/j.jcis.2004.08.132

[17] Romero-Sanz, I., Bocanegra, R., de la Mora, J. F., and Gamero-Castaño, M., "Source of Heavy Molecular Ions Based on Taylor Cones of Ionic Liquids Operating in the Pure Ion Evaporation Regime," *Journal of Applied Physics*, Vol. 94, No. 5, 2003, pp. 3599–3605. doi:10.1063/1.1598281

[18] Chiu, Y.-H., Gaeta, G., Heine, T., Dressler, R., and Levandier, D., "Analysis of the Electrospray Plume from the EMI-Im Propellant Externally Wetted on a Tungsten Needle," *42nd AIAA/ASME/SAE/ASEE Joint Propulsion Conference and Exhibit*, AIAA Paper 2006-5010, 2006.

[19] Legge, R. S. J., Lozano, P., and Martinez-Sanchez, M., "Fabrication and Characterization of Porous Metal Emitters for Electrospray Thrusters," *International Electric Propulsion Conference*, IEPC Paper 2007-145, Electric Rocket Propulsion Soc., Fairview Park, OH, 2007.

[20] Coffman, C., Perna, L., Li, H., and Lozano, P. C., "On the Manufacturing and Emission Characteristics of a Novel Borosilicate Electrospray Source," *49th AIAA/ASME/SAE/ASEE Joint Propulsion Conference*, AIAA Paper 2013-4035, 2013.

[21] Perna, L. E., Mier Hicks, F., Coffman, C. S., Li, H., and Lozano, P. C., "Progress Toward Demonstration of Remote, Autonomous Attitude Control of a CubeSat Using Ion Electrospray Propulsion Systems," *48th AIAA/ASME/SAE/ASEE Joint Propulsion Conference and Exhibit*, AIAA Paper 2012-4289, 2012.

[22] Brikner, N., and Lozano, P. C., "The Role of Upstream Distal Electrodes in Mitigating Electrochemical Degradation of Ionic Liquid Ion Sources," *Applied Physics Letters*, Vol. 101, No. 19, 2012, Paper 193504. doi:10.1063/1.4766293

[23] Masuyama, K., and Lozano, P., "Electrical Double Layers in Electrospray Propulsion," *International Electric Propulsion Conference*, IEPC Paper 2015-178, Electric Rocket Propulsion Soc., Fairview Park, OH, 2015.

[24] Brikner, N., "On the Identification and Mitigation of Life-Limiting Mechanisms of Ionic Liquid Ion Sources Envisaged for Propulsion of Microspacecraft," Ph.D. Dissertation, Dept. of Aeronautics and Astronautics, Massachusetts Inst. of Technology, Cambridge, MA, 2015.

[25] Krejci, D., Mier Hicks, F., Fucetola, C., Lozano, P., Hsu Schouten, A., and Martel, F., "Design and Characterization of a Scalable ion Electrospray Propulsion System," *34th International Electric Propulsion Conference*, IEPC Paper 20150149, Electric Rocket Propulsion Soc., Fairview Park, OH, 2015.

[26] Perez-Martinez, C. S., and Lozano, P. C., "Visualization of Beams from Ionic Liquid Ion Sources for Focused Ion Beam Applications," *Journal of Vacuum Science & Technology B*, Vol. 30, No. 6, Nov.–Dec. 2012, Paper 06F601. doi:10.1116/1.4745187

[27] Haag, T. W., "Thrust Stand for Pulsed Plasma Thrusters," *Review of Scientific Instruments*, Vol. 68, No. 5, 1997, pp. 2060–2067. doi:10.1063/1.1148097

[28] Guerra-Garcia, C., Krejci, D., and Lozano, P., "Spatial Uniformity of the Current Emitted by an Array of Passively Fed Electrospray Porous Emitters," *Journal of Physics D: Applied Physics*, Vol. 49, No. 11, 2016, Paper 115503. doi:10.1088/0022-3727/49/11/115503

[29] Perez-Martinez, C. S., and Lozano, P. C., "Visualization of Beams from Ionic Liquid Ion Sources for Focused Ion Beam Applications," *Journal of Vacuum Science and Technology B*, Vol. 30, No. 6, Nov.–Dec. 2012, Paper 06F601. doi:10.1116/1.4745187

[30] Miller, C., and Lozano, P., "The Effects of Metastable Solvated Ions on Electrospray Ion Thruster Efficiency," *34th International Electric Propulsion Conference*, 2015.

[31] Courtney, D., and Shea, H., "Fragmentation in Time-of-Flight Spectrometry-Based Calculations of Ionic Electrospray Thruster Performance," *Journal of Propulsion and Power*, Vol. 31, No. 5, 2015, pp. 1500–1504. doi:10.2514/1.B35837

[32] Legge, R. S. J., and Lozano, P. C., "Electrospray Propulsion Based on Emitters Microfabricated in Porous Metals," *Journal of Propulsion and Power*, Vol. 27, No. 2, 2011, pp. 485–495. doi:10.2514/1.50037

[33] Romero-Sanz, I., de Carcer, I., and de la Mora, J. F., "Ionic Propulsion Based on Heated Taylor Cones of Ionic Liquids," *Journal of Propulsion and Power*, Vol. 21, No. 2, 2005, pp. 239–242. doi:10.2514/1.5493

[34] Alonso-Matilla, R., Fernández-Garca, J., Congdon, H., and de la Mora, J. F., "Search for Liquids Electrospraying the Smallest Possible Nanodrops in Vacuo," *Journal of Applied Physics*, Vol. 116, No. 22, 2014, Paper 224504. doi:10.1063/1.4901635

[35] Zhang, S., Sun, N., He, X., Lu, X., and Zhang, X., "Physical Properties of Ionic Liquids: Database and Evaluation," *Journal of Physics and Chemical Reference Data*, Vol. 35, No. 4, 2006, pp. 1475–1517. doi:10.1063/1.2204959

[36] Whitaker, S., "Flow in Porous Media I: A Theoretical Derivation of Darcy's Law," *Transport in Porous Media*, Vol. 1, No. 1, 1986, pp. 3–25.

[37] Lozano, P., and Martinez-Sanchez, M., "Efficiency Estimation of EMI-BF4 Ionic Liquid Electrospray Thrusters," *41st AIAA/ASME/SAE/ASEE Joint Propulsion Conference and Exhibit*, AIAA Paper 2005-4388, 2005.

[38] Chiu, Y.-H., Austin, B. L., Dressler, R. A., Levandier, D., Murray, P. T., Lozano, P., and Sanchez, M. M., "Mass Spectrometric Analysis of Colloid Thruster Ion Emission from Selected Propellants," *Journal of Propulsion and Power*, Vol. 21, No. 3, 2005, pp. 416–423. doi:10.2514/1.9690

[39] Fedkiw, T., "Characterization of an Iodine-Based Ionic Liquid Ion Source and Studies on Ion Fragmentation," M.S. Thesis, Dept. of Aeronautics and Astronautics, Massachusetts Inst. of Technology, Cambridge, MA, 2010.

[40] Lozano, P. C., "Studies on the Ion-Droplet Mixed Regime in Colloid Thrusters," Ph.D. Dissertation, Dept. of Aeronautics and Astronautics, Massachusetts Inst. of Technology, Cambridge, MA, 2003.

M. Walker
Associate Editor